(Received 16 February 2026, Accepted 9 March 2026, Scheduled 7 April 2026)

Error-Aware Joint Position and Excitation Optimization for Shaped Beam Linear Array Synthesis

Le Trong Phuoc Bui*

Department of Mathematics, Electric Power University, 235 Hoang Quoc Viet, Nghia Do, Hanoi, Vietnam

ABSTRACT: This study addresses the synthesis of shaped beams for linear antenna arrays under dynamic range ratio constraints on excitation amplitudes. When hardware limitations restrict excitation freedom, conventional methods suffer significant sidelobe degradation. The proposed approach jointly optimizes the element positions and excitations through iterative second-order cone programming. A distinguishing feature is the error-aware constraint formulation, which incorporates linearization error bounds, ensuring actual pattern compliance with the beam mask at each iteration. Adaptive trust-region control based on actual-to-predicted improvement ratios ensures robust convergence. Numerical experiments with flat-top and cosecant-squared beams demonstrated 7–12 dB sidelobe improvement over excitation-only methods under strict amplitude constraints. Compared with particle swarm optimization, the proposed method achieves superior sidelobe suppression while being orders of magnitude faster.

1. INTRODUCTION

Shaped beam synthesis, which involves designing radiation patterns to approximate prescribed amplitude profiles over specified angular regions, is essential in radar, communication, sonar, and remote sensing [1, 2]. Applications include flat-top beams for cellular base stations and cosecant-squared beams for airborne radar [3, 4]. Unlike pencil beams, which require only sidelobe suppression, shaped beams impose both upper and lower bounds on the mainlobe, making the problem more challenging.

For fixed array geometries, shaped beam synthesis reduces to excitation optimization, which can be solved via second-order cone programming (SOCP) or semidefinite programming [5–8]. Iterative SOCP has been applied to conformal array synthesis [9], alternating convex optimization to unequally spaced arrays with minimum spacing constraints [10], hybrid sub-array beamforming [11], and optimal monopulse beamforming for airborne radars [12]. However, when the dynamic range ratio (DRR) — the ratio of maximum to minimum excitation amplitude — is constrained due to power amplifier limitations [13, 14], excitation-only methods may lack sufficient freedom for low sidelobes. Several studies have addressed DRR-constrained synthesis [15–17], but all operate on fixed geometries.

To enlarge the design space, the element positions can be jointly optimized. Position optimization via Taylor-expansion linearization has been applied to pencil beam synthesis with fixed excitations [18, 19] and sparse array synthesis for element count minimization [20–28]. Joint position and excitation optimization has also been investigated through sparseness-constrained optimization [29], Bayesian compressive sampling [30], matrix mapping with differential evolution [31], and hybrid PSO with convex programming [32]. Alternating convex optimization with minimum spacing constraints has been proposed in [10]. Metaheuristic methods, such as genetic algorithms and particle swarm optimization [33–36], can jointly optimize the positions and excitations but suffer from high computational costs and difficulty in handling dense mask constraints. However, joint position-excitation optimization for shaped beams with DRR constraints has not been addressed via convex optimization, and existing perturbation methods lack error-aware trust-region control.

Regarding robustness to errors and uncertainties, Monte Carlo methods have been used to determine error tolerance in array elements [37]. Interval-based particle swarm optimization has been applied to robust mask-constrained synthesis [38]. Interval analysis combined with convex optimization has addressed optimal robust array synthesis [39], and robust pencil beam synthesis under position uncertainty has been studied in [40]. These works address manufacturing or positioning uncertainties, whereas the error-awareness in the present work targets the linearization approximation error inherent in the iterative optimization process itself — a fundamentally different source of error that has not been addressed in the prior literature.

This paper proposes an error-aware joint optimization method with the following contributions:

1. **Joint perturbation framework.** We formulate a unified SOCP that simultaneously optimizes the position perturbations $\boldsymbol{\varepsilon} \in \mathbb{R}^N$ and excitation perturbations $\Delta\mathbf{w} \in \mathbb{C}^N$. Both the mainlobe lower bound $|F(u)| \geq L(u)$ and the DRR lower bound $|w_n| \geq a_{\min}$ — which are non-convex — are handled via phase projection, yielding a fully convex subproblem at each iteration.

* Corresponding author: Le Trong Phuoc Bui (phuocblt@epu.edu.vn).

2. **Error-aware trust-region mechanism.** We derive explicit linearization error bounds and incorporate them as constraint backoffs to ensure actual pattern compliance despite approximation errors. The trust-region adapts based on the ratio between the actual and predicted improvement [41], expanding when the model is accurate and shrinking otherwise, a feature absent in prior perturbation methods.
3. **DRR-aware insight.** Numerical experiments demonstrate that the position optimization improvement is the greatest under tight DRR constraints (7–12 dB sidelobe level (SLL) improvement at DRR $\leq$ 2) and diminishes as the DRR becomes unconstrained.

The remainder of this paper is organized as follows. Section 2 presents the problem formulation. Section 3 describes the proposed method. Section 4 presents the numerical results. Finally, Section 5 concludes the paper.

2. PROBLEM FORMULATION

Consider a linear antenna array with N isotropic elements located along the x-axis. Each element n ($n = 1, \ldots, N$) is characterized by its position d_n (normalized by wavelength λ) and complex excitation $w_n = a_n e^{j\psi_n}$, where a_n and ψ_n denote the amplitude and phase, respectively. The far-field radiation pattern in the u-domain, where $u = \sin\theta$ and θ is the angle measured from the broadside, is given by

$$F(u) = \sum_{n=1}^{N} w_n e^{j2\pi d_n u}, \quad u \in [-1, 1]. \tag{1}$$

In vector form, this can be written as $F(u) = \mathbf{w}^T \mathbf{s}(u)$, where $\mathbf{w} = [w_1, \ldots, w_N]^T$ is the excitation vector, and $\mathbf{s}(u) = [e^{j2\pi d_1 u}, \ldots, e^{j2\pi d_N u}]^T$ is the steering vector.

The u-domain is partitioned into three regions: the mainlobe Ω_m, the sidelobe Ω_s, and the transition regions. For a symmetric flat-top beam centered at the broadside, $\Omega_m = \{u : |u| \leq u_{ml}\}$ and $\Omega_s = \{u : |u| \geq u_{sl}\}$, where $u_{ml} < u_{sl}$. For asymmetric beams, such as cosecant-squared patterns, Ω_m and Ω_s can be arbitrary disjoint subsets of $[-1, 1]$. The beam synthesis requirements are specified through amplitude masks: in the mainlobe, $L(u) \leq |F(u)| \leq U(u)$ for all $u \in \Omega_m$, where $L(u)$ and $U(u)$ define the lower and upper bounds, respectively; in the sidelobe, $|F(u)| \leq \rho$ for all $u \in \Omega_s$, where ρ is the sidelobe level to be minimized. For a flat-top beam with a ripple tolerance δ, we set $L(u) = 1 - \delta$ and $U(u) = 1 + \delta$. For a cosecant-type beam with a shaped region $[u_{\text{start}}, u_{\text{end}}]$, the bounds follow a power-law shape function $G(u) = (u_{\text{start}}/u)^{\alpha}$, where the exponent α determines the taper rate.

Practical implementations impose constraints on the excitation amplitudes owing to the limitations of power amplifiers. The dynamic range ratio (DRR) is defined as DRR $= \max_n |w_n| / \min_n |w_n|$. Constraining DRR $\leq R$ is equivalent to requiring

$$a_{\min} \leq |w_n| \leq a_{\max}, \quad \forall n, \tag{2}$$

where $a_{\max} = R \cdot a_{\min}$. When R is small (strict DRR), the excitation freedom is significantly limited, making it difficult to achieve low sidelobes through excitation optimization.

The joint position and excitation optimization problem for shaped beam synthesis is formulated as

$$\begin{aligned}
\min_{\mathbf{w},\mathbf{d},\rho} \quad & \rho && && (3)\\
\text{s.t.} \quad & |F(u_i)| \leq \rho, && \forall u_i \in \Omega_s && (4)\\
& |F(u_i)| \leq U(u_i), && \forall u_i \in \Omega_m && (5)\\
& |F(u_i)| \geq L(u_i), && \forall u_i \in \Omega_m && (6)\\
& |w_n| \leq a_{\max}, && \forall n && (7)\\
& |w_n| \geq a_{\min}, && \forall n && (8)\\
& d_n - d_{n-1} \geq d_{\min}, && n = 2, \ldots, N && (9)
\end{aligned}$$

where $\mathbf{d} = [d_1, \ldots, d_N]^T$ is the position vector, and $d_{\min}$ is the minimum element spacing to avoid mutual coupling. This problem is non-convex owing to three factors: (i) the pattern $F(u)$ contains the bilinear product $w_n \cdot e^{j2\pi d_n u}$, coupling excitations and positions; (ii) the mainlobe lower bound (6) defines a non-convex feasible region (exterior of a disk); and (iii) the DRR lower bound (8) is similarly non-convex. The proposed method addresses these challenges through iterative linearization with error-aware constraints, as described in the following sections.

3. PROPOSED METHOD

The proposed approach solves non-convex problems (3)–(9) through iterative linearization. At each iteration k, given the current solution $(\mathbf{w}^{(k)}, \mathbf{d}^{(k)})$, we seek small perturbations $\Delta\mathbf{w}$ and $\boldsymbol{\varepsilon}$ such that $\mathbf{w} = \mathbf{w}^{(k)} + \Delta\mathbf{w}$ and $\mathbf{d} = \mathbf{d}^{(k)} + \boldsymbol{\varepsilon}$ reduce the sidelobe level. By keeping the perturbations small, the problem can be linearized and solved as a second-order cone program (SOCP).

Substituting the perturbed variables into (1) and applying the first-order Taylor expansion $e^{j2\pi\varepsilon_n u} \approx 1 + j2\pi\varepsilon_n u$ for small ε_n, the pattern becomes

$$\tilde{F}(u) = F^{(k)}(u) + \Delta\mathbf{w}^T \boldsymbol{\alpha}(u) + \boldsymbol{\varepsilon}^T \boldsymbol{\beta}(u), \tag{10}$$

where $F^{(k)}(u) = \sum_n w_n^{(k)} e^{j2\pi d_n^{(k)} u}$ is the current pattern, and the sensitivity vectors are

$$\alpha_n(u) = e^{j2\pi d_n^{(k)} u}, \tag{11}$$

$$\beta_n(u) = j2\pi u \cdot w_n^{(k)} \cdot e^{j2\pi d_n^{(k)} u}. \tag{12}$$

The linearized pattern $\tilde{F}(u)$ is affine in the optimization variables $(\Delta\mathbf{w}, \boldsymbol{\varepsilon})$, enabling convex formulation.

The non-convex constraints (6) and (8) are handled using phase projection. For the mainlobe lower bound, instead of requiring $|\tilde{F}(u_i)| \geq L(u_i)$, we enforce

$$\text{Re}\left\{\tilde{F}(u_i) \cdot e^{-j\varphi_i^{(k)}}\right\} \geq L(u_i), \tag{13}$$

where $\varphi_i^{(k)} = \angle F^{(k)}(u_i)$ is the current pattern's phase. This projects the constraint onto a half-plane aligned with the current

phase, converting it into a linear constraint. Similarly, for the DRR lower bound,

$$\mathrm{Re}\left\{(w_n^{(k)} + \Delta w_n) \cdot e^{-j\psi_n^{(k)}}\right\} \geq a_{\min}, \tag{14}$$

where $\psi_n^{(k)} = \angle w_n^{(k)}$.

The linearization introduces an approximation error. For the Taylor expansion, $|e^{jx} - 1 - jx| \leq x^2/2$, yielding the pattern error bound

$$|\Delta F_{\mathrm{err}}(u)| \leq 2\pi^2 u^2 \Delta_{\mathrm{pos}}^2 \left(W_\Sigma + N\Delta_w\right) + 2\pi|u|N\Delta_w\Delta_{\mathrm{pos}}, \tag{15}$$

where $W_\Sigma = \sum_n |w_n^{(k)}|$, and Δ_{pos} and Δ_w are the trust-region radii bounding $|\varepsilon_n|$ and $|\Delta w_n|$, respectively. This bound accounts for both the Taylor truncation and the neglected bilinear term $\Delta w_n \cdot \varepsilon_n$.

To clarify the derivation, the exact perturbed pattern is $F(u) = \sum_n (w_n^{(k)} + \Delta w_n) e^{j2\pi(d_n^{(k)} + \varepsilon_n)u}$. Subtracting the linearized approximation $\tilde{F}(u)$ from (10), the error $\Delta F_{\mathrm{err}}(u) = F(u) - \tilde{F}(u)$ consists of two components: (i) the Taylor remainder from each element, $w_n^{(k)}(e^{j2\pi\varepsilon_n u} - 1 - j2\pi\varepsilon_n u)$, bounded by $|w_n^{(k)}| \cdot 2\pi^2\varepsilon_n^2 u^2$ using $|e^{jx} - 1 - jx| \leq x^2/2$; and (ii) the bilinear cross-term $\Delta w_n(e^{j2\pi\varepsilon_n u} - 1)$, bounded by $|\Delta w_n| \cdot (2\pi^2\varepsilon_n^2 u^2 + 2\pi|\varepsilon_n u|)$ using $|e^{jx} - 1| \leq |x| + x^2/2$. Summing over all N elements and replacing $|\varepsilon_n| \leq \Delta_{\mathrm{pos}}$ and $|\Delta w_n| \leq \Delta_w$ yields (15).

The key contribution is the incorporation of this error bound directly into the constraints. For the mainlobe constraints where the mask must be strictly satisfied, we apply a backoff:

$$|\tilde{F}(u_i)| \leq U(u_i) - \delta(u_i), \quad \forall u_i \in \Omega_m, \tag{16}$$

$$\mathrm{Re}\{\tilde{F}(u_i)e^{-j\varphi_i^{(k)}}\} \geq L(u_i) + \delta(u_i), \quad \forall u_i \in \Omega_m, \tag{17}$$

where $\delta(u_i)$ is the error bound (15), evaluated at u_i. This ensures that the actual pattern satisfies the mask, even when the linearization is imperfect. For the sidelobe constraint, backoff is not applied: at zero perturbation ($\Delta\mathbf{w} = \mathbf{0}$, $\boldsymbol{\varepsilon} = \mathbf{0}$), the constraint $|\tilde{F}(u_i)| \leq \rho$ must be feasible with $\rho = \rho^{(k)}$, which is violated if backoff is applied at the sidelobe peaks. Instead, a ratio test was used to validate the actual improvement after each iteration.

The complete SOCP solved at each iteration is:

$$\begin{aligned}
\min_{\Delta\mathbf{w},\boldsymbol{\varepsilon},\rho} \quad & \rho \\
\text{s.t.} \quad & |\tilde{F}(u_i)| \leq \rho, && \forall u_i \in \Omega_s \\
& |\tilde{F}(u_i)| \leq U(u_i) - \delta(u_i), && \forall u_i \in \Omega_m \\
& \mathrm{Re}\{\tilde{F}(u_i)e^{-j\varphi_i^{(k)}}\} \geq L(u_i) + \delta(u_i), && \forall u_i \in \Omega_m \\
& |w_n^{(k)} + \Delta w_n| \leq a_{\max}, && \forall n \\
& \mathrm{Re}\{(w_n^{(k)} + \Delta w_n)e^{-j\psi_n^{(k)}}\} \geq a_{\min}, && \forall n \\
& |\varepsilon_n| \leq \Delta_{\mathrm{pos}},\ |\Delta w_n| \leq \Delta_w, && \forall n \\
& \varepsilon_n - \varepsilon_{n-1} \geq d_{\min} - (d_n^{(k)} - d_{n-1}^{(k)}), && n \geq 2
\end{aligned} \tag{18}$$

All constraints are either second-order cone or linear, making this a standard SOCP.

The complete algorithm is summarized in Algorithm 1.

Algorithm 1 Error-Aware Joint Position and Excitation Optimization

Require: Uniform linear array (ULA) positions $\mathbf{d}^{(0)}$, DRR bounds $[a_{\min}, a_{\max}]$, tolerances ϵ_{tol}, $k_{\max}$
Ensure: Optimized $(\mathbf{w}^*, \mathbf{d}^*)$

Solve excitation-only SOCP on ULA $\rightarrow \mathbf{w}^{(0)}$
Clip amplitudes: $|w_n| \leftarrow \mathrm{clip}(|w_n|, a_{\min}, a_{\max})$
Initialize trust-region radii Δ_{pos}, Δ_w
for $k = 1, 2, \ldots, k_{\max}$ **do**
  Compute error bound $\delta(u)$ via (15)
  Solve SOCP (18) $\rightarrow (\Delta\mathbf{w}, \boldsymbol{\varepsilon}, \rho_{\mathrm{SOCP}})$
  Evaluate actual SLL: $\rho_{\mathrm{actual}} \leftarrow \max_{u_i \in \Omega_s} |F(u_i)|$
  Compute ratio: $r \leftarrow (\rho^{(k-1)} - \rho_{\mathrm{actual}})/(\rho^{(k-1)} - \rho_{\mathrm{SOCP}})$
  if $r > 0$ **then**
    Accept: $\mathbf{w}^{(k)} \leftarrow \mathbf{w}^{(k-1)} + \Delta\mathbf{w}$, $\mathbf{d}^{(k)} \leftarrow \mathbf{d}^{(k-1)} + \boldsymbol{\varepsilon}$
    if $r > 0.75$ **then**
      Expand trust-region: $\Delta_{\mathrm{pos}} \leftarrow 1.5\Delta_{\mathrm{pos}}$
    else if $r < 0.25$ **then**
      Shrink trust-region: $\Delta_{\mathrm{pos}} \leftarrow 0.5\Delta_{\mathrm{pos}}$
    end if
  else
    Reject step, shrink: $\Delta_{\mathrm{pos}} \leftarrow 0.25\Delta_{\mathrm{pos}}$
  end if
  if $\|\boldsymbol{\varepsilon}\|_\infty < \epsilon_{\mathrm{tol}}$ **and** $\|\Delta\mathbf{w}\|_\infty < \epsilon_{\mathrm{tol}}$ **then**
    break
  end if
end for
return $(\mathbf{w}^{(k)}, \mathbf{d}^{(k)})$

After solving the SOCP, the trust-region is adapted based on the ratio $r = (\rho^{(k-1)} - \rho_{\mathrm{actual}})/(\rho^{(k-1)} - \rho_{\mathrm{SOCP}})$, where $\rho^{(k-1)}$ is the current SLL before the update and ρ_{actual} is the true sidelobe level computed from the full (non-linearized) pattern. If $r > 0.75$, the model is accurate, and the trust-region expands; if $r < 0.25$, it shrinks; if $r \leq 0$, the step is rejected, and the trust-region is reduced significantly. This adaptive mechanism ensures a robust convergence without manual tuning.

The algorithm is initialized with excitation-only optimization on a uniform linear array (ULA) and then clips the amplitudes to satisfy the DRR constraints. The main loop iterates until convergence, defined by $\|\boldsymbol{\varepsilon}\|_\infty < \epsilon_{\mathrm{tol}}$, $\|\Delta\mathbf{w}\|_\infty < \epsilon_{\mathrm{tol}}$, and relative SLL change below ϵ_{tol}.

Regarding computational complexity, each SOCP subproblem (18) involves $2N + 1$ real optimization variables (N complex excitation perturbations, N real position perturbations, and the sidelobe level ρ) and $O(M + N)$ second-order cone and linear constraints, where M is the number of angular sampling points. Standard interior-point solvers handle each subproblem in polynomial time. The total computational cost is $O(K \cdot T_{\mathrm{SOCP}})$, where K is the number of outer iterations (typically 50–100) and T_{SOCP} is the per-subproblem solve time. As demonstrated in Table 5, the total computation time scales near-linearly with N, ranging from 10.8 s for $N = 16$ to 21.3 s for $N = 48$, confirming practical scalability for moderate-to-large arrays.

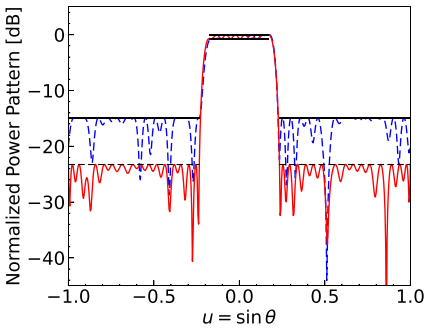

FIGURE 1. Radiation pattern comparison for $N = 40$ elements with DRR $= 3$. Blue dashed line: Method A (excitation-only on ULA), achieving SLL $= -14.89$ dB. Red solid line: Method B (proposed joint optimization), achieving SLL $= -23.27$ dB. Gray shaded region: mainlobe mask with ± 0.36 dB ripple tolerance ($L = 0.96, U = 1.04$). Horizontal dotted lines indicate the respective sidelobe levels. Position optimization provides ΔSLL $= 8.38$ dB improvement.

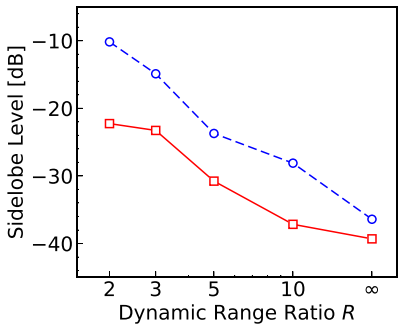

FIGURE 2. Sidelobe level versus dynamic range ratio R for $N = 40$ flat-top beam synthesis. Blue circles with dashed line: Method A (excitation-only optimization). Red squares with solid line: Method B (proposed joint optimization). The gap between curves represents ΔSLL, the improvement from position optimization. Maximum ΔSLL (12.09 dB) occurs at $R = 2$; minimum ΔSLL (2.90 dB) at $R = \infty$.

4. NUMERICAL RESULTS

The proposed method was validated through five test cases examining: (i) the relationship between position optimization improvement and DRR constraint, (ii) convergence behavior and error-aware mechanism effectiveness, (iii) generalization to asymmetric-shaped beams, (iv) comparison with metaheuristic optimization, and (v) the effect of array size. To quantify the benefit of position optimization, the metric $\Delta\text{SLL} = \text{SLL}_A - \text{SLL}_B$ is defined, where SLL_A and SLL_B denote the sidelobe levels achieved by Method A (excitation-only optimization on ULA) and Method B (proposed joint optimization), respectively. A positive ΔSLL indicates that the proposed method outperformed the baseline.

4.1. Simulation Setup

All simulations considered linear arrays with element positions normalized by wavelength ($\lambda = 1$). The initial configuration was a uniform linear array (ULA) with inter-element spacing $d_0 = 0.5\lambda$. The minimum element spacing constraint is set to $d_{\min} = 0.4\lambda$ to avoid mutual coupling effects. The angular domain is discretized into $M = 500$ uniformly spaced points over $u \in [-1, 1]$.

Two beam shapes were considered. The *flat-top beam* follows the setup in [17], with a symmetric mainlobe region $\Omega_m = \{u : |u| \leq 0.174\}$ (corresponding to $|\theta| < 10°$) and sidelobe region $\Omega_s = \{u : |u| \geq 0.233\}$ (corresponding to $|\theta| > 13.5°$). The mainlobe mask is defined by $L(u) = 0.96$ and $U(u) = 1.04$, yielding a ripple tolerance of ± 0.36 dB. The *cosecant-squared beam* has an asymmetric-shaped mainlobe over $\Omega_m = [0.05, 0.60]$ with an amplitude following $G(u) \propto 1/u^{0.926}$ (producing a 10 dB taper) and a ripple tolerance of ± 0.5 dB.

The choice of $M = 500$ sampling points yields an angular resolution of $\Delta u = 0.004$, which is significantly finer than the mainlobe-to-sidelobe transition width ($u_{sl} - u_{ml} = 0.059$ for the flat-top beam). Numerical tests with $M = 1000$ produced negligible SLL change (< 0.01 dB), confirming that $M = 500$ provides sufficient sampling density for reliable mask compliance and optimization results.

The trust-region is initialized with $\Delta_{\text{pos}}^{(0)} = 0.08\lambda$ and $\Delta_w^{(0)} = 0.25 \cdot \bar{a}$, where $\bar{a}$ is the mean excitation amplitude. Convergence is declared when perturbations and relative SLL change fall below $\epsilon_{\text{tol}} = 10^{-4}$, or after $k_{\max} = 100$ iterations. All SOCP subproblems were solved using MOSEK via CVXPY [42] on a single-core CPU.

4.2. DRR Sweep

The first test case validates the main claim that the position optimization improvement increases as the DRR constraint tightens. A 40-element array synthesizing a flat-top beam was evaluated with $R \in \{2, 3, 5, 10, \infty\}$, where $a_{\min} = 1.0$ and $a_{\max} = R \cdot a_{\min}$.

Table 1 summarizes these results. At $R = 2$, Method A achieves only -10.17 dB owing to the severely constrained excitation freedom, whereas Method B achieves -22.26 dB, yielding ΔSLL $= 12.09$ dB. As R increases, Method A improves from -10.17 dB to -36.41 dB (a 26.24 dB range), whereas Method B improves from -22.26 to -39.31 dB (17.05 dB range). At $R = \infty$ (unconstrained DRR), ΔSLL reduces to 2.90 dB. The total element displacement remained in the range 7.5–11λ across all DRR values.

TABLE 1. Sidelobe level versus DRR for $N = 40$ flat-top beam synthesis. SLL_A: excitation-only optimization on ULA. SLL_B: proposed joint optimization. ΔSLL: improvement from position optimization. Displacement: total element displacement $\sum_n |d_n^{\text{final}} - d_n^{\text{ULA}}|$.

R	SLL_A (dB)	SLL_B (dB)	ΔSLL (dB)	Displacement (λ)
2	-10.17	-22.26	12.09	9.85
3	-14.89	-23.27	8.38	7.54
5	-23.72	-30.77	7.06	7.59
10	-28.11	-37.16	9.05	7.58
∞	-36.41	-39.31	2.90	11.29

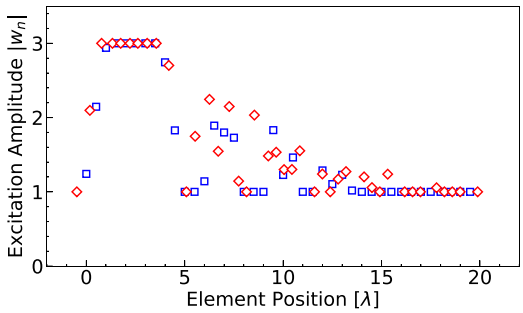

FIGURE 3. Element layout comparison for $N = 40$, DRR $= 3$. Horizontal axis: element position d_n (in wavelengths). Vertical axis: excitation amplitude $|w_n|$. Blue circles: initial configuration (ULA with DRR-clipped excitations from Method A). Red diamonds: optimized configuration (Method B result). Total displacement: $\sum_n |d_n^{\text{final}} - d_n^{\text{ULA}}| = 7.54\lambda$. Elements near the array edges exhibit larger displacements.

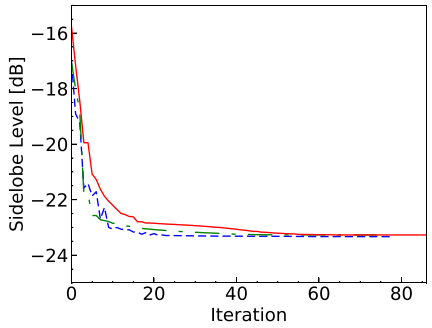

FIGURE 4. SLL convergence versus iteration for three trust-region strategies ($N = 40$, $R = 3$). Green dotted line: fixed decay ($\gamma = 0.9$). Blue dashed line: ratio test only. Red solid line: full error-aware (proposed). All strategies converge to a similar final SLL (≈ -23.3 dB). The full error-aware strategy requires slightly more iterations (87 vs 75–79) due to the conservative constraint backoff, but guarantees mask compliance throughout convergence.

Figure 1 shows the radiation pattern at $R = 3$. Method A exhibits sidelobes at -14.89 dB owing to the limited amplitude tapering capability under the DRR constraint. Method B achieves -23.27 dB while satisfying all the mainlobe and DRR constraints. Fig. 2 summarizes the relationship between SLL and R. At $R = 2$, Method A achieves only -10.17 dB, whereas Method B reaches -22.26 dB, yielding a maximum $\Delta\text{SLL} = 12.09$ dB. The divergence between the curves at low R and convergence at high R confirm that position optimization is most effective when the excitation freedom is constrained by hardware limitations. Fig. 3 compares the initial and optimized array configurations, showing that the position optimization redistributes elements with larger displacements near the array edges.

4.3. Convergence Analysis

The second test case validates the error-aware trust-region mechanisms. Three trust-region strategies were compared for a 40-element array with $R = 3$ and a flat-top beam: (i) fixed decay with $\gamma = 0.9$ (trust-region shrinks by factor γ each iteration: $\Delta_{\text{pos}}^{(k+1)} = \gamma \cdot \Delta_{\text{pos}}^{(k)}$), (ii) ratio test only (adaptive trust-region without constraint backoff), and (iii) full error-aware (proposed: adaptive trust-region with constraint backoff).

Table 2 summarizes this comparison. All three strategies achieve similar final SLL (≈ -23.3 dB), indicating that the constraint backoff does not compromise the optimization performance. The critical difference lies in the mask violation behavior. The fixed decay and ratio test only strategies violate the mainlobe constraints in 99% and 100% of the iterations, respectively, relying on eventual convergence to restore compliance. The ratio test only strategy results in five grid points violating the upper bound in the final pattern. In contrast, the full error-aware strategy maintained zero mask violations throughout all 87 iterations.

Figure 4 shows the SLL convergence trajectory. The full error-aware strategy exhibits a slightly slower initial descent owing to the conservative backoff, but achieves the same final SLL. Fig. 5 displays the per-iteration diagnostics for the proposed method, demonstrating that the linearized model closely predicts the actual improvement ($\rho_{\text{SOCP}} \approx \rho_{\text{actual}}$) when the trust-region is appropriately sized. Five-step rejections occur when the model overestimates the improvement. Fig. 6 compares the initial and optimized array configurations, showing that the position optimization redistributes elements with larger displacements near the array edges. Fig. 7 confirms that only the full error-aware strategy guarantees mainlobe mask compliance in the final pattern.

TABLE 2. Trust-region strategy comparison for $N = 40$, $R = 3$, flat-top beam. Viol. Iters: iterations with mainlobe mask violation during convergence. Final Viol: grid points violating mainlobe bounds in the final pattern out of 86 total mainlobe points.

Strategy	SLL (dB)	Iters	Viol Iters	Final Viol
Fixed decay ($\gamma = 0.9$)	-23.33	79	78/79	0/86
Ratio test only	-23.27	75	75/75	5/86
Full error-aware	-23.27	87	0/87	0/86

4.4. Cosecant Beam

The third test case demonstrates the generalization of the framework to asymmetric beams. A 40-element array synthesizing a cosecant-squared beam was evaluated with the same DRR values as in Section 4.2.

TABLE 3. Sidelobe level versus DRR for $N = 40$ cosecant-squared beam synthesis.

R	SLL_A (dB)	SLL_B (dB)	ΔSLL (dB)	Displacement (λ)
2	-25.27	-32.58	7.31	8.81
3	-23.22	-30.86	7.64	6.21
5	-26.56	-35.52	8.96	6.10
10	-24.51	-33.16	8.65	6.85
∞	-42.81	-43.49	0.69	1.96

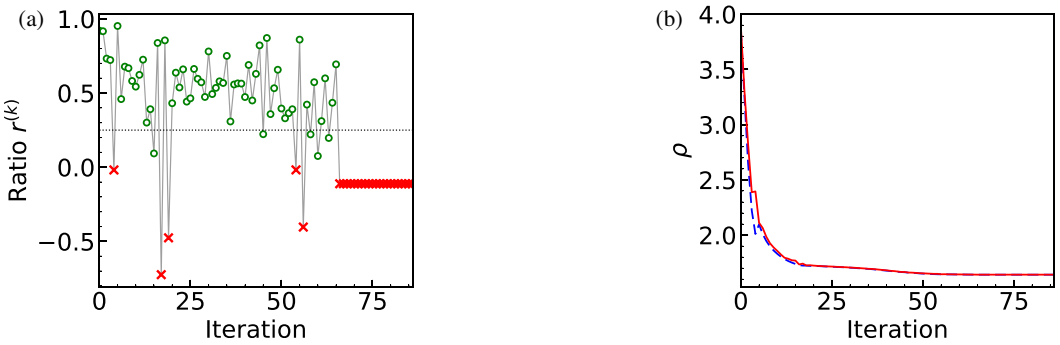

FIGURE 5. Per-iteration diagnostics for the proposed full error-aware strategy. (a) Ratio $r^{(k)}$ versus iteration: green circles indicate accepted steps ($r > 0$), red crosses indicate rejected steps ($r \leq 0$). Horizontal dotted line at $r = 0.25$ marks the threshold between trust-region expansion ($r > 0.75$) and contraction ($r < 0.25$). Rejections occur at iterations 4, 17, 19, 54, 56. (b) SLL comparison: blue dashed line shows ρ_{SOCP} (predicted by linearized model), red solid line shows ρ_{actual} (measured on the actual pattern). Near-perfect overlap validates linearization accuracy within the trust-region.

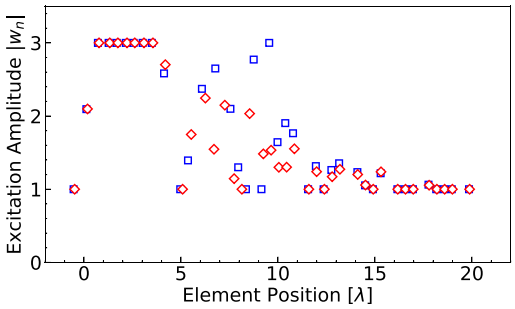

FIGURE 6. Element layout comparison for $N = 40$, $R = 3$. Horizontal axis: element position d_n (in wavelengths). Vertical axis: excitation amplitude $|w_n|$. Blue circles: initial configuration (ULA with DRR-clipped excitations from Method A). Red diamonds: optimized configuration (Method B result). Total displacement: $\sum_n |d_n^{\text{final}} - d_n^{\text{ULA}}| = 7.54\lambda$. Elements near array edges exhibit larger displacements, consistent with their greater influence on sidelobe formation.

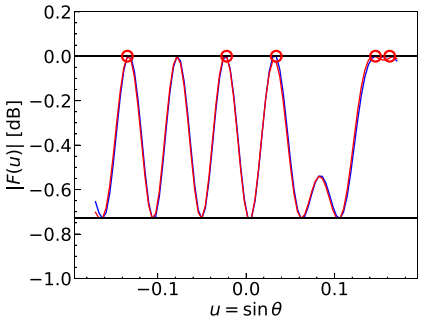

FIGURE 7. Mainlobe mask compliance comparison for the final optimized patterns. (a) Ratio test only strategy: pattern magnitude in mainlobe region ($|u| \leq 0.174$). Red circles mark 5 grid points where $|F(u)|$ exceeds the upper bound $U(u) = 1.04$ (+0.36 dB). Violations are on the order of 10^{-5} dB above the bound. (b) Full error-aware strategy (proposed): zero violations across all 86 mainlobe grid points. The constraint backoff $\delta(u)$ guarantees mask compliance despite linearization errors.

Table 3 summarizes these results. For $R \leq 10$, ΔSLL ranges from 7.31 to 8.96 dB, which is consistent with the flat-top beam results. At $R = \infty$, ΔSLL reduces to 0.69 dB, confirming that the DRR-dependent value of the position optimization extends to arbitrarily shaped beams. The cosecant beam achieves lower absolute SLL values (-23 to -43 dB) than the flat-top beam (-10 to -39 dB) owing to the asymmetric mainlobe that naturally suppresses the sidelobes on one side.

Figures 8 and 9 show the radiation pattern at $R = 3$ and the SLL versus R summary, respectively. The framework correctly enforces the shaped mainlobe mask with varying amplitude bounds across the mainlobe region. The position optimization improvement was consistent across beam shapes, validating the generality of the proposed approach.

4.5. Comparison with PSO

In the fourth test case, the proposed method is benchmarked against particle swarm optimization (PSO). Both methods were applied to a 40-element array with $R = 3$ and a flat-top beam. The PSO was configured with 200 particles, 10,000 iterations per run, and 20 independent runs (best result selected).

TABLE 4. Method comparison for $N = 40$, $R = 3$, flat-top beam. Ripple: maximum deviation from unity in the mainlobe. Time: total computation time on single-core CPU.

Method	SLL (dB)	Ripple (dB)	Time (s)	Displacement (λ)
Excitation-only	-14.89	0.73	12.0	0.00
Proposed	-23.27	0.73	12.4	7.33
PSO	-15.46	0.73	28364.5	0.26

Table 4 summarizes this comparison. The proposed method achieves an SLL $= -23.27$ dB, outperforming PSO by 7.81 dB (-23.27 vs -15.46 dB). The proposed method is 2,287 times faster than PSO (12.4 s vs 28364.5 s $\approx$ 7.9 hours). Despite 20 independent runs, PSO achieves only a 0.57 dB improvement over excitation-only optimization and barely utilizes position degrees of freedom (0.26λ vs 7.33λ total displacement).

Figure 10 compares the radiation patterns. The PSO results exhibited higher sidelobes throughout the sidelobe region. The proposed method maintains uniform sidelobe suppression and strict mask compliance. The deterministic nature of the pro-

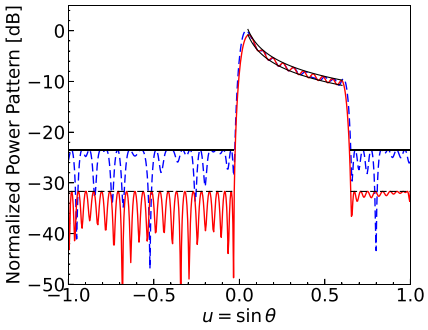

FIGURE 8. Cosecant-squared beam radiation pattern for $N = 40$, DRR $= 3$. Blue dashed line: Method A (SLL $= -23.22$ dB). Red solid line: Method B (SLL $= -30.86$ dB). Gray shaded region: shaped mainlobe mask following cosecant-squared profile from $u = 0.05$ to $u = 0.60$ with 10 dB taper and ± 0.5 dB ripple tolerance. The asymmetric mainlobe extends from $\theta \approx 2.9°$ to $\theta \approx 36.9°$. ΔSLL $= 7.64$ dB.

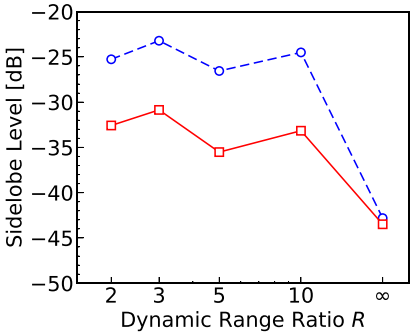

FIGURE 9. Sidelobe level versus DRR for cosecant-squared beam synthesis. Blue circles with dashed line: Method A. Red squares with solid line: Method B. Consistent ΔSLL of 7–9 dB is achieved for $R \leq 10$. At $R = \infty$, ΔSLL reduces to 0.69 dB, confirming that the position optimization benefit is DRR-dependent regardless of beam shape.

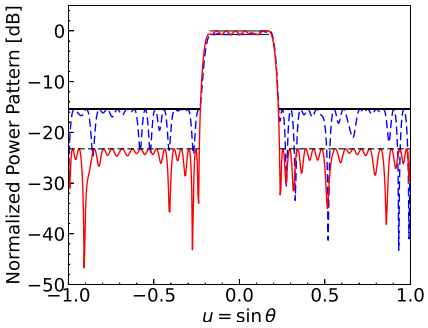

FIGURE 10. Radiation pattern comparison for $N = 40$, DRR $= 3$. Blue dashed line: PSO result (SLL $= -15.46$ dB, 200 particles $\times$ 10000 iterations $\times$ 20 runs). Red solid line: proposed method (SLL $= -23.27$ dB). Gray shaded region: mainlobe mask with ± 0.36 dB ripple tolerance. Horizontal dotted lines indicate SLL levels. The proposed method achieves 7.81 dB better SLL while being 2287$\times$ faster (12.4 s vs 28364.5 s).

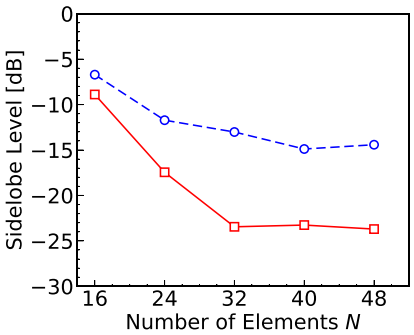

FIGURE 11. Sidelobe level versus number of elements N for $R = 3$, flat-top beam. Blue circles with dashed line: Method A (excitation-only optimization). Red squares with solid line: Method B (proposed joint optimization). Both methods improve with increasing N due to additional degrees of freedom. The gap between curves (ΔSLL) increases from 2.18 dB at $N = 16$ to 10.44 dB at $N = 32$, then stabilizes around 8–9 dB for larger arrays.

posed approach also provides reproducibility, whereas the PSO results vary between runs.

4.6. Array Size Variation

The fifth test case evaluates the performance versus the array size. The proposed method is applied to arrays with $N \in \{16, 24, 32, 40, 48\}$ elements, $R = 3$, and a flat-top beam with the same configuration as in Section 4.2 ($u_{ml} = 0.1$, $u_{sl} = 0.15$, $\delta = 0.04$).

TABLE 5. Performance versus number of elements for $R = 3$, flat-top beam. Time: total computation time including all iterations.

N	SLL$_A$ (dB)	SLL$_B$ (dB)	ΔSLL (dB)	Time (s)
16	−6.71	−8.89	2.18	10.8
24	−11.72	−17.45	5.73	13.6
32	−13.02	−23.45	10.44	16.5
40	−14.89	−23.27	8.38	18.2
48	−14.42	−23.70	9.28	21.3

Table 5 summarizes these results. Both methods generally improve with increasing N owing to the additional degrees of freedom: Method A improves from -6.71 to -14.89 dB as N increases from 16 to 40, with slight degradation at $N = 48$ (-14.42 dB) owing to beam width constraints. Method B improves from -8.89 dB to -23.70 dB. The improvement ΔSLL increases from 2.18 dB at $N = 16$ to 10.44 dB at $N = 32$, and then stabilizes at approximately 8–9 dB for larger arrays. The computation time scales near-linearly with N: 10.8 s ($N = 16$) to 21.3 s ($N = 48$).

Figure 11 shows the SLL versus N summary. The consistent benefit of position optimization across array sizes confirms the consistent benefit of the proposed framework for different array sizes.

5. CONCLUSION

An error-aware joint position and excitation optimization method for shaped beam synthesis under DRR constraints was presented. The method formulates the problem as an iterative SOCP with two key mechanisms: constraint backoff incorporating linearization error bounds, and adaptive trust-region

control based on actual-to-predicted improvement ratios. These mechanisms guarantee mainlobe mask compliance throughout convergence while maintaining the optimization performance.

Numerical experiments on flat-top and cosecant-squared beams demonstrated that the position optimization improvement was the highest under tight DRR constraints and diminished as the DRR became unconstrained. At DRR $= 2$, the proposed method achieves 12.09 dB SLL improvement over excitation-only optimization; at DRR $= \infty$, the improvement reduces to 2.90 dB. Compared with PSO, the proposed method achieves a 7.81 dB better SLL while being over 2,000 times faster and guaranteeing constraint satisfaction. The framework scales efficiently with the array size, with the computation time increasing near-linearly from 10.8 s ($N = 16$) to 21.3 s ($N = 48$).

The results indicate that the joint position-excitation optimization is most valuable when hardware limitations restrict the excitation freedom. In future work, the framework may be extended to planar arrays, and the mutual coupling effects may be incorporated. For planar array extension, the position perturbation vector generalizes from $\boldsymbol{\varepsilon} \in \mathbb{R}^N$ to $(\boldsymbol{\varepsilon}_x, \boldsymbol{\varepsilon}_y) \in \mathbb{R}^{2N}$, and the steering vector becomes a function of two angular variables (u, v). The SOCP structure is preserved, though the number of optimization variables and angular sampling points increases substantially. The current simulations employ isotropic radiating elements, which is a common assumption for validating synthesis algorithms. Incorporating realistic element patterns — such as embedded element patterns obtained from full-wave electromagnetic simulations — would require replacing the isotropic steering vector $e^{j2\pi d_n u}$ with element-specific radiation functions $g_n(\theta)e^{j2\pi d_n u}$, where $g_n(\theta)$ accounts for the individual element pattern including mutual coupling effects. The proposed linearization and error-aware framework remains applicable in this setting, as the sensitivity vectors (11)–(12) would be modified accordingly while preserving the affine structure of the linearized pattern.

REFERENCES

[1] Lebret, H. and S. Boyd, "Antenna array pattern synthesis via convex optimization," *IEEE Transactions on Signal Processing*, Vol. 45, No. 3, 526–532, 1997.

[2] Murino, V. and A. Trucco, "Three-dimensional image generation and processing in underwater acoustic vision," *Proceedings of the IEEE*, Vol. 88, No. 12, 1903–1948, 2000.

[3] Elliott, R. and G. Stern, "A new technique for shaped beam synthesis of equispaced arrays," *IEEE Transactions on Antennas and Propagation*, Vol. 32, No. 10, 1129–1133, 1984.

[4] Isernia, T., O. M. Bucci, and N. Fiorentino, "Shaped beam antenna synthesis problems: Feasibility criteria and new strategies," *Journal of Electromagnetic Waves and Applications*, Vol. 12, No. 1, 103–138, 1998.

[5] Nai, S. E., W. Ser, Z. L. Yu, and H. Chen, "Beampattern synthesis for linear and planar arrays with antenna selection by convex optimization," *IEEE Transactions on Antennas and Propagation*, Vol. 58, No. 12, 3923–3930, 2010.

[6] Wang, F., V. Balakrishnan, P. Y. Zhou, J. J. Chen, R. Yang, and C. Frank, "Optimal array pattern synthesis using semidefinite programming," *IEEE Transactions on Signal Processing*, Vol. 51, No. 5, 1172–1183, 2003.

[7] Fuchs, B., "Synthesis of sparse arrays with focused or shaped beampattern via sequential convex optimizations," *IEEE Transactions on Antennas and Propagation*, Vol. 60, No. 7, 3499–3503, 2012.

[8] Fuchs, B., A. Skrivervik, and J. R. Mosig, "Shaped beam synthesis of arrays via sequential convex optimizations," *IEEE Antennas and Wireless Propagation Letters*, Vol. 12, 1049–1052, 2013.

[9] Tsui, K. M. and S. C. Chan, "Pattern synthesis of narrowband conformal arrays using iterative second-order cone programming," *IEEE Transactions on Antennas and Propagation*, Vol. 58, No. 6, 1959–1970, 2010.

[10] You, P., Y. Liu, S.-L. Chen, K. D. Xu, W. Li, and Q. H. Liu, "Synthesis of unequally spaced linear antenna arrays with minimum element spacing constraint by alternating convex optimization," *IEEE Antennas and Wireless Propagation Letters*, Vol. 16, 3126–3130, 2017.

[11] Rocca, P., L. Manica, R. Azaro, and A. Massa, "A hybrid approach to the synthesis of subarrayed monopulse linear arrays," *IEEE Transactions on Antennas and Propagation*, Vol. 57, No. 1, 280–283, 2009.

[12] Gottardi, G., L. Poli, P. Rocca, A. Montanari, A. Aprile, and A. Massa, "Optimal monopulse beamforming for side-looking airborne radars," *IEEE Antennas and Wireless Propagation Letters*, Vol. 16, 1221–1224, 2017.

[13] Fuchs, B. and S. Rondineau, "Array pattern synthesis with excitation control via norm minimization," *IEEE Transactions on Antennas and Propagation*, Vol. 64, No. 10, 4228–4234, 2016.

[14] Buttazzoni, G. and R. Vescovo, "Synthesis of co-polar and cross-polar patterns with dynamic range ratio reduction for phase-only reconfigurable arrays," in *2012 6th European Conference on Antennas and Propagation (EUCAP)*, 2623–2627, Prague, Czech Republic, 2012.

[15] Lei, S., H. Hu, P. Tang, B. Chen, J. Tian, W. Yang, and X. Qiu, "Power-gain pattern synthesis of array antenna with dynamic range ratio restriction," *IEEE Antennas and Wireless Propagation Letters*, Vol. 18, No. 12, 2691–2695, 2019.

[16] Lin, Z., H. Hu, S. Lei, R. Li, J. Tian, and B. Chen, "Low-sidelobe shaped-beam pattern synthesis with amplitude constraints," *IEEE Transactions on Antennas and Propagation*, Vol. 70, No. 4, 2717–2731, 2022.

[17] Li, L., X. Zhang, and Z. He, "Beampattern synthesis with dynamic range ratio constraint via sequential convex optimization," *IEEE Antennas and Wireless Propagation Letters*, Vol. 23, No. 10, 3227–3231, 2024.

[18] Fuchs, B., A. Skrivervik, and J. R. Mosig, "Synthesis of uniform amplitude focused beam arrays," *IEEE Antennas and Wireless Propagation Letters*, Vol. 11, 1178–1181, 2012.

[19] Lei, S., H. Hu, B. Chen, P. Tang, J. Tian, and X. Qiu, "An array position refinement algorithm for pencil beam pattern synthesis with high-order Taylor expansion," *IEEE Antennas and Wireless Propagation Letters*, Vol. 18, No. 9, 1766–1770, 2019.

[20] Yan, F., P. Yang, F. Yang, and T. Dong, "Synthesis of planar sparse arrays by perturbed compressive sampling framework," *IET Microwaves, Antennas & Propagation*, Vol. 10, No. 11, 1146–1153, 2016.

[21] Gu, B., Y. Chen, R. Jiang, and X. Liu, "Optimization of sparse cross array synthesis via perturbed convex optimization," *Sensors*, Vol. 20, No. 17, 4929, 2020.

[22] Zhao, D., X. Liu, W. Chen, and Y. Chen, "Optimized design for sparse cross arrays in both near-field and far-field," *IEEE Jour-*

nal of Oceanic Engineering, Vol. 44, No. 3, 783–795, 2019.

[23] Lin, Z., Y. Chen, X. Liu, R. Jiang, B. Shen, and X.-X. Guo, "Optimized design for sparse arrays in 3-D imaging sonar systems based on perturbed Bayesian compressive sensing," *IEEE Sensors Journal*, Vol. 20, No. 10, 5554–5565, 2020.

[24] Yan, F., P. Yang, F. Yang, L. Zhou, and M. Gao, "Synthesis of pattern reconfigurable sparse arrays with multiple measurement vectors FOCUSS method," *IEEE Transactions on Antennas and Propagation*, Vol. 65, No. 2, 602–611, 2017.

[25] Liu, Y., Y. Yang, F. Han, Q. H. Liu, and Y. J. Guo, "Improved beam-scannable ultra-wideband sparse antenna arrays by iterative convex optimization based on raised power series representation," *IEEE Transactions on Antennas and Propagation*, Vol. 68, No. 7, 5696–5701, 2020.

[26] Liang, L., C. Jin, H. Li, J. Liu, Y. Jiang, and J. Zhou, "A hybrid algorithm of orthogonal perturbation method and convex optimization for beamforming of sparse antenna array," *Electromagnetics*, Vol. 40, No. 4, 227–243, 2020.

[27] Liang, L., Y. Jiang, J. Liu, H. Li, and J. Zhou, "Pattern synthesis of time-modulated sparse array by an OPM-CVX algorithm," *Mathematical Problems in Engineering*, Vol. 2020, No. 1, 5491921, 2020.

[28] Yang, F., S. Yang, Y. Chen, S. Qu, and J. Hu, "Synthesis of sparse antenna arrays subject to constraint on directivity via iterative convex optimization," *IEEE Antennas and Wireless Propagation Letters*, Vol. 20, No. 8, 1498–1502, 2021.

[29] Zhang, W., L. Li, and F. Li, "Reducing the number of elements in linear and planar antenna arrays with sparseness constrained optimization," *IEEE Transactions on Antennas and Propagation*, Vol. 59, No. 8, 3106–3111, 2011.

[30] Oliveri, G., M. Carlin, and A. Massa, "Complex-weight sparse linear array synthesis by Bayesian compressive sampling," *IEEE Transactions on Antennas and Propagation*, Vol. 60, No. 5, 2309–2326, 2012.

[31] Liu, H., H. Zhao, W. Li, and B. Liu, "Synthesis of sparse planar arrays using matrix mapping and differential evolution," *IEEE Antennas and Wireless Propagation Letters*, Vol. 15, 1905–1908, 2016.

[32] Oliveri, G. and T. Moriyama, "Hybrid PSO-CP technique for the synthesis of non-uniform linear arrays with maximum directivity," *Journal of Electromagnetic Waves and Applications*, Vol. 29, No. 1, 113–123, 2015.

[33] Haupt, R. L., "Thinned arrays using genetic algorithms," *IEEE Transactions on Antennas and Propagation*, Vol. 42, No. 7, 993–999, 1994.

[34] Hooker, J. W. and R. K. Arora, "Optimal thinning levels in linear arrays," *IEEE Antennas and Wireless Propagation Letters*, Vol. 9, 771–774, 2010.

[35] Trucco, A., "Thinning and weighting of large planar arrays by simulated annealing," *IEEE Transactions on Ultrasonics, Ferroelectrics, and Frequency Control*, Vol. 46, No. 2, 347–355, 1999.

[36] Liu, X., F. Zhou, H. Zhou, and X. Tian, "Synthesis of extreme sparse array for real-time 3D acoustic imaging," *Electronics Letters*, Vol. 51, No. 11, 803–804, 2015.

[37] Lee, J., Y. Lee, and H. Kim, "Decision of error tolerance in array element by the Monte Carlo method," *IEEE Transactions on Antennas and Propagation*, Vol. 53, No. 4, 1325–1331, 2005.

[38] Manica, L., N. Anselmi, P. Rocca, and A. Massa, "Robust mask-constrained linear array synthesis through an interval-based particle SWARM optimisation," *IET Microwaves, Antennas & Propagation*, Vol. 7, No. 12, 976–984, 2013.

[39] Rocca, P., N. Anselmi, and A. Massa, "Optimal synthesis of robust beamformer weights exploiting interval analysis and convex optimization," *IEEE Transactions on Antennas and Propagation*, Vol. 62, No. 7, 3603–3612, 2014.

[40] Tian, J., S. Lei, Z. Lin, Y. Gao, H. Hu, and B. Chen, "Robust pencil beam pattern synthesis with array position uncertainty," *IEEE Antennas and Wireless Propagation Letters*, Vol. 20, No. 8, 1483–1487, 2021.

[41] Nocedal, J. and S. J. Wright, *Numerical Optimization*, 2nd ed., Springer, New York, NY, USA, 2006.

[42] Diamond, S. and S. Boyd, "CVXPY: A Python-embedded modeling language for convex optimization," *Journal of Machine Learning Research*, Vol. 17, No. 83, 1–5, 2016.